A calcium sensor discovered in Bluetongue virus non-structural protein 2 is critical for virus replication

Shah Kamranur Rahman[1], Adeline Kerviel[1#], Bjorn-Patrick Mohl[1], Yao He[2], Z. Hong Zhou[2] and Polly Roy[1*]

[1]Department of Infection Biology, London School of Hygiene and Tropical Medicine, London WC1E 7HT UK. [2]California NanoSystems Institute, and Department of Microbiology, Immunology & Molecular Genetics, UCLA, CA 90095, USA

Running title: ***Discovery of Ca^{2+} binding protein in BTV***

Keywords: Bluetongue Virus, Ca^{2+} binding protein, Nonstructural protein, Viral inclusion bodies, Casein kinase II subunit alpha, Reverse genetics, Circular dichroism, CryoEM

*To whom correspondence should be addressed: Polly Roy: Department of Infection Biology, London School of Hygiene and Tropical Medicine, London WC1E 7HT UK; polly.roy@lshtm.ac.uk; Tel. +44 20 79272324.

[#] Present address: Laboratory of Host-Pathogen Dynamics, National Heart, Lung and Blood Institute, National Institutes of Health, Bethesda, MD, USA

ABSTRACT

Many viruses use specific viral proteins to bind calcium ions (Ca^{2+}) for stability or to modify host cell pathways, however, to date no Ca^{2+} binding protein has been reported in Bluetongue virus (BTV), the causative agent of Bluetongue disease in livestock. Here, using a comprehensive bioinformatics screening, we identified a putative EF-hand-like Ca^{2+} binding motif in the carboxyl terminal region of BTV non-structural phosphoprotein 2 (NS2). Subsequently, using a recombinant NS2, we demonstrated that NS2 binds Ca^{2+} efficiently and that Ca^{2+} binding was perturbed when the Asp and Glu residues in the motif were substituted by Alanine. Using Circular dichroism analysis, we found that Ca^{2+} binding by NS2 triggered a helix-to-coil secondary structure transition. Further, cryo-electron microscopy in presence of Ca^{2+}, revealed that NS2 forms helical oligomers which, when aligned with the N-terminal domain crystal structure, suggest an N-terminal domain which wraps around the C-terminal domain in the oligomer. Further, an *in vitro* kinase assay demonstrated that Ca^{2+} enhanced the phosphorylation of NS2 significantly. Importantly, mutations introduced at the Ca^{2+} binding site in the viral genome by reverse genetics failed to allow recovery of viable virus and that the NS2 phosphorylation level and assembly of VIBs were reduced. Together, our data suggest that NS2 is a dedicated Ca^{2+} binding protein and that calcium sensing acts as a trigger for VIB assembly, which in turn facilitates virus replication and assembly.

Importance

After entering the host cells viruses use cellular host factors to ensure a successful virus replication process. For replication in infected cells members of *Reoviridae* family form an inclusion body like structure known as viral inclusion bodies (VIB) or viral factories. Bluetongue virus (BTV) forms VIBs in infected cells through non-structural protein 2 (NS2), a phosphoprotein. An important regulatory factor critical for VIB formation is phosphorylation of NS2. In our study, we discovered a characteristic calcium binding EF hand like motif in NS2 and found that the calcium binding preferentially affects phosphorylation level of the NS2 and has a role in regulating VIB assembly.

Introduction

Bluetongue virus (BTV) of the Orbivirus genus in the *Reoviridae* family is an insect-borne animal pathogen. BTV is vectored by *Culicoides* spp. and causes infection in vertebrate hosts (sheep, cattle and goat) in many parts of the world that has considerable economic impact. The non-enveloped BTV particle is a complex icosahedral structure, consisting of seven structural proteins (VP1 to VP7) that are organised in an outer capsid and an inner capsid (core). The outer capsid is composed of two major proteins, VP2 and VP5, and is responsible for attachment and membrane penetration. Both proteins are lost during endocytosis and the inner core is subsequently released into the cytoplasm. The BTV core consists of the remaining five proteins and the viral genome of 10 double-stranded RNA (dsRNA) segments. In addition to 7 structural proteins, also four non-structural proteins, NS1-NS4 are synthesised during virus replication. Two of these are major non-structural (NS) proteins, NS1 and NS2, which are synthesised during early infection, and each plays an essential role in virus replication. The third NS protein, NS3/NS3A is a trans-membrane protein and facilitates release of the newly assembled BTV (1-3), NS4 is newly identified and its function is still not fully characterised and a fifth putative non-structural protein (4-6). Previously we reported that NS3 interacts with cellular exocytic pathway protein p11 (S100A10), a protein known to facilitate Ca^{2+} uptake, suggesting indirect involvement of NS3 with Ca^{2+} related signaling pathways (1,7). Several enveloped and non-enveloped viruses employ their proteins (Tat, gp120, nef of HIV-1, HBx of HBV, NSP4 of rotavirus, P7 of HCV) to modulate cellular Ca^{2+} haemostasis for ensuring a successful viral life cycle (8,9). For example, rotavirus expresses membrane-localising NSP4 protein that binds Ca^{2+} and influences Ca^{2+} homeostasis (9). BTV and rotavirus belong to the same family, however unlike rotavirus NSP4, a Ca^{2+} binding protein in BTV is yet unknown.

In this study, we used bioinformatics to identify whether any of the BTV proteins has Ca^{2+} binding motif. We identified EF hand-like motif in NS2 which is the only viral encoded phosphoprotein and essential for replication (10). The 357 amino acid (aa) long NS2 is the major component of viral inclusion bodies (VIBs), the sites for viral capsid assembly and genome packaging. The identified EF hand-like motif in NS2 was comparable to those found in other member proteins of EF-hand superfamily that are characteristically known for Ca^{2+} binding. Using recombinant purified protein, together with biochemical and biophysical analysis we demonstrated that Ca^{2+} binding changes

the secondary structural conformation of NS2. Moreover, our cryo-electron microscopy (CryoEM) analysis of NS2 oligomer in presence of Ca^{2+} exhibited a helical architecture. By site-specific targeted mutagenesis in the recombinant NS2 and in the replicating viral genome by reverse genetics, we identified the specific Ca^{2+} binding site of NS2 and demonstrated its importance in NS2 phosphorylation level, formation of VIBs and virus replication. Altogether, our results suggest that Ca^{2+} sensing by NS2 influence NS2 phosphorylation and may be involved in the regulation of VIB assembly/disassembly a process critical for virus replication and the release of newly assembled cores from VIBs (2, 11).

Results

Computer based sequence analysis of BTV proteins reveals putative Ca^{2+} binding site in NS2

In order to identify putative Ca^{2+} binding motif, we used SMART motif search program for each of the eleven BTV proteins, including seven structural proteins (VP1-VP7) and four NS proteins (12). In our linear sequence search, only NS2, exhibited signature residues (200-300aa) of EF hand like motif, found in Ca^{2+} binding proteins of EF hand superfamily (Fig. 1). In particular, presence of acidic amino acid, Asp and Glu in the region 250-262aa, suggests the calcium binding potential of this segment of NS2 (Fig. 1A) (13-14). However, we found that the relative positioning of signature residues of EF hand motif and Ca^{2+} binding residues identified in NS2 are different than that has been observed in typical EF hand containing calcium binding proteins (CaBP), thus making this putative motif less obvious. These acidic residues in NS2 are continuous rather than alternate as found in the case of standard EF hand motifs (Fig. 1A). These clusters (250-262aa) of Asp (D) and Glu (E) of NS2 resemble more like "Ca^{2+} bowl" found in BK (big potassium) channels (15-21). Further, these Asp and Glu residues are highly conserved among different BTV serotypes indicating that the putative Ca^{2+} binding motif is likely to be important for BTV replication (Fig.1B).

Demonstration of Ca^{2+} binding ability of NS2 oligomers and helix-to-coil transition in secondary structure

To validate our bioinformatics analysis, we expressed NS2 in *E coli,* in a non-phosphorylated form, purified and analysed by SDS-PAGE gel (Fig. 2A). Purified NS2, free of any bound metals and pre-treated with chelex-100, was examined for Ca^{2+}

binding activity during metal titration experiment through Circular Dichroism (CD). The changes in intrinsic far-UV CD spectra were recorded, as the direct measure of Ca^{2+} binding to purified NS2, without (apo) or with (holo) Ca^{2+} at the increasing concentrations of Ca^{2+}, from 5 μM to 10 mM, to calculate the dissociation constant, Kd. NS2 showed Kd value of 53.9 (± 8.4) μM for Ca^{2+} binding. In comparison, another divalent ion Mg^{2+} when tested for NS2 binding in a parallel titration experiment with same concentrations range, showed a Kd value of 2.48 (± 0.4) mM suggesting a weaker binding of Mg^{2+} as compared to Ca^{2+} (Fig. 2B, 2C).

Also, NS2 formed stably intact oligomers and eluted at an elution volume on the size exclusion column corresponding to an estimated molecular weight of ~440 kDa suggesting decamers (Fig. 2D). The stability of the oligomers was not dependent on Ca^{2+} binding as both apo NS2 and NS2-Ca^{2+} eluted at the same elution volume. To investigate further the effect of Ca^{2+} on NS2 secondary structure, which was largely alpha helical, we analyzed the far UV CD spectrum at optimum Ca^{2+} concentrations based on the prior titration experiments (Fig. 3A). NS2 showed dose dependent changes in secondary structure elements in the presence of Ca^{2+} (Fig. 3B).

The effect of Ca^{2+} on NS2 spectra was diminished in the presence of 0.4μM EGTA consistent with chelation of the Ca^{2+} ion (Fig. 3A) (18). Importantly, at a higher molar concentration of Ca^{2+} ([Ca^{2+}] = 44.67 μM), NS2 showed a very different CD spectrum (Fig. 3B) suggestive of a helix-to-coil transition in response to Ca^{2+} binding, as shown by other Ca^{2+} binding proteins from the EF hand superfamily, for example, Calmodulin (22). The change of helix to coil also prompted us to analyze *in silico* predicted secondary structure of NS2 near the Ca^{2+} binding site. The computer program PSIPRED suggested helix, beta strands and coils in NS2 protein in different regions, however IUPred2, a specific program to predict intrinsic unfolded regions or coil, suggested unfolded regions are mainly located near and at the Ca^{2+} binding site (Fig. 4A, 4B) (23,24).

Identification of Ca^{2+} binding site of NS2

To determine which Asp and Glu residues in the predicted region 250-262aa, are responsible for Ca^{2+} binding activity, we generated a series of recombinant NS2 mutant proteins by site-specific mutagenesis targeting these three sites (Fig. 1, Table 1). The amino acid substitutions were introduced, by replacing negatively charged

residues Asp (D) and Glu (E) with Ala (A), a neutral amino acid, which would have minimal impact on overall protein structure, unlike deletion mutants. The NS2 alanine mutant proteins such as $DDDE_{250\text{-}3}AAAA$ (A1), $ED_{256\text{-}7}AA$ (A2) and $DDE_{260\text{-}2}AAA$ (A3) respectively, were then purified and analysed by gel electrophoresis to determine that each mutant protein expressed was stable and equivalent to wild type NS2 (wtNS2) (Fig. 4C). Further, size exclusion chromatography analysis of each protein, showed that all three mutant proteins appeared equivalent to wtNS2, with an approximate molecular mass of ~ 440kDa (data not shown). Prior to investigation of Ca^{2+} binding activity of NS2 mutants, we compared their CD spectra with the wtNS2 and calculated the estimated secondary structure elements using BeStSel program (25) (Fig. 5A). There was no significant change in the percentage of helix, beta strands or turns in mutants indicating no major changes in the secondary structure elements (Fig. 5B). CD titration analysis of each NS2 mutant protein was then performed in presence of Ca^{2+}. The two mutants A2 and A3 showed the Kd values (~64 μM, ~44 μM respectively) similar to that of wtNS2 (Kd value ~54 μM) suggesting not much change in the Ca^{2+} binding activities of mutants A2, A3 (Fig. 5C, 5D). However, the mutant A1 showed weak Ca^{2+} binding as reflected from an increase in Kd values to ~ 150 μM (Fig. 5C, 5D). Thus, the four alanine residues (250-253aa) substitutions of Glu and Asp residues have affected Ca^{2+} binding ability significantly, indicating the three consecutive Glu and an Asp DDDE, at aa250-253 are important for Ca^{2+} binding activity of NS2.

Ca^{2+} binding enhances phosphorylation level of NS2 in vitro

Since Ca^{2+} binding site (aa250-253) is in juxtaposition of serine residues (S249, S259), known for phosphorylation modification, it was more likely that Ca^{2+} mediated transition in the secondary structure elements could affect the level of NS2 phosphorylation. Therefore, we undertook an *in vitro* kinase assay for NS2 phosphorylation, a modification required for VIB assembly (2,11). Since Casein Kinase II alpha (CK2α) is responsible for NS2 phosphorylation, we used CK2α and purified unmodified NS2 as substrate (11). Our data showed that for the fixed ratio of substrate and kinase, much higher signal of γ-[^{32}P] labelled-phosphate-group transfer to NS2 was achieved in the presence of Ca^{2+} ions than that in the presence of Mg^{2+} ions (Fig. 6A, 6B). Presence of Mg^{2+} ion showed a minimum basal level of phosphorylation of

substrate NS2, determined at two different metal ion concentrations. Taken together, of these two ions, Ca^{2+} binding specifically increases phosphorylation level of purified NS2 protein. Further, we did not observe any increase in the activity of CK2α for another substrate (e.g. Glutathione S-transferase, GST) in the presence of Ca^{2+} ions (control, data not shown). To confirm further, the specificity of Ca^{2+} binding activity on NS2 phosphorylation, we assessed the three NS2 mutants A1, A2 and A3 as substrates, for CK2α kinase assay in presence of Ca^{2+} (Fig. 6C). The NS2 mutants A2, A3 did not show any significantly change in the level of phosphorylation as compared to the wtNS2. In contrast, NS2 mutant A1 showed a marked decrease in the level of phosphorylation suggesting a critical role of calcium binding site on phosphorylation of the protein by the CK2α kinase (Fig. 6C).

Subunits in NS2 oligomers are arranged in helical fashion

Since NS2-Ca^{2+} interaction changes the percentage of helix in NS2, we investigated whether this change has any destabilizing effect on the oligomeric state of NS2. To this end, purified NS2 in the presence of Ca^{2+} was visualized by cryo-electron microscopy (cryoEM). In total, 159,361 particle images were selected from 2,712 cryoEM micrographs and subjected to image classification to obtain 2D class averages. Particles with clear helical organizational features were observed in some 2D classes (Fig. 7). The pitch and outer diameter of those helical particles were measured to be 75 Å and 91 Å, respectively (Fig. 7A & 7B), matching the parameters of the helical structure of NS2 N-terminal domain observed by X-ray crystallography (26). Modeling of the crystal structure into this cryoEM average suggests that a single turn of the NS2 helix is contributed by 10 monomers (Fig. 7C). The full-length NS2 oligomer showed a helical overall structure and the N-terminal domain of NS2 contributes to the formation of the helical configuration. 2D classes with clear “ring-like” feature could be further assigned to helical NS2 oligomers on their front view (Fig. 7B & 7D), since their outer diameter are the same as “helical particles” (Fig. 7A). Interestingly, clear density could be observed inside the “ring”, which corresponds to the center of NS2 helical shape (Fig. 7B). Considering the C-terminal end of the N-terminal domain points towards the inside of the helical particle (K160, labeled as purple sphere in Fig. 7C), we propose that the C-terminal domains of NS2 are located inside the helical structure formed by the N-terminal domains of individual subunits of the helical oligomers of NS2.

Disruption of putative Ca^{2+} binding residues in NS2 affects virus replication.

Above data demonstrated that NS2 possesses specific Ca^{2+} binding site. Such specific calcium binding activity is likely to influence virus fitness in infected cells. To address this issue, we introduced site directed substitution mutations in BTV genome and studied the effect using reverse genetics (RG) as described previously (27). A set of alanine substitutions mutations on NS2 were designed (Table 1). Three of these mutations in the encoding S8 segment were the same NS2 sites, A1 ($DDDE_{250-3}AAAA$), A2 ($ED_{256-7}AA$) or A3 ($DDE_{260-2}AAA$). In addition, two multi-sites mutations in S8, A1+2 ($DDDE_{250-3}AAAA$ + $ED_{256-7}AA$), and A1+2+3 ($DDDE_{250-3}AAAA+ED_{256-7}AA+DDE_{260-2}AAA$) were created (Table1) to assess if other two sites (A2, A3) have influence on Ca^{2+} binding residues 250-253aa during virus replication. For a negative control, we used an available NS2 phosphorylation mutant SAA, in which phosphorylated serine sites (S249 and S259) were previously substituted by alanine residues (SAA) that perturbed virus replication (2,11). When BSR cells were transfected with each mutant S8 together with 9 remaining RNA segments for virus recovery by reverse genetics, only A2 and A3 mutant viruses were recovered successfully but not A1 or the others that included A1 mutation (A1+2, A1+2+3) (Fig. 8). Subsequently each RNA cocktail was then used to transfect BS8 cells, which stably express wtNS2 protein (Segment 8) to validate the RG experiment and viability of mutant viruses. In parallel, BSR cells were also transfected similarly for comparison. Cells were fixed 48 hours post transfection. The mutant virus A2 and A3, formed plaques both in BSR and BS8 cells with similar phenotypes of wt virus and titers (PFU/mL values ~7 log10) suggesting no apparent change due to these mutations (Fig. 8). In contrast, the mutant viruses A1, A1+2 and A1+2+3 and the negative control SAA mutant virus showed typical plaque forming phenotype only in the NS2 complementary BS8 cells. These data highlighted the critical role of Asp and Glu residues at 250-253aa (site A1), and further validated the RG experiment of the mutant S8 that failed to recover in normal BSR cells (Fig. 8).

To investigate further the failure of virus recovery with the mutation at the A1 site, we assessed whether Asp and Glu (250-53aa) residues identified for Ca^{2+} sensing was critical for the NS2-triggered VIBs formation, the sites of virus assembly. BSR cells were therefore infected, with either WT virus or one of the three mutant viruses A1 ($DDDE_{250-3}AAAA$), A2 ($ED_{256-7}AA$) or A3 ($DDE_{260-2}AAA$) recovered from the NS2

complementary BS8 cells and VIBs morphology in the infected BSR cells was visualized by confocal microscopy. Changes in the average size (area in μm^2) of VIBs in cells infected with WT and mutant viruses were quantified. Cells infected with A1 mutant virus showed smaller VIBs as compared to the VIBs in the WT virus infected cells, however mutants A2, A3 showed no significant change in average size of VIBs (Fig. 9). The A1 mutant virus after infection in cell showed ~1.6-fold smaller VIBs than WT virus infected cells, (Fig. 9B). Taken together, these data suggest that Ca^{2+} binding Asp and Glu residues in aa250-253 has role in VIB formation and virus replication, consistent with the *in vitro* Ca^{2+} binding and kinase assay data (Fig. 2, Fig.6).

NS2 phosphorylation decreases following disruption of putative Ca^{2+} binding motifs in NS2.

To obtain direct evidence on whether the defective Ca^{2+} binding motif resulting diminished VIBs was due to poor phosphorylation of NS2, BSR cells were infected with WT and the mutant viruses in addition to NS2 phosphorylation negative mutant SAA, following optimized protocol for BTV (11). BSR cells were infected with the viruses at MOI = 1 and NS2 purified by immuno-precipitation (11). Pull-downs were confirmed by western blot and the gel stained with Pro-Q Diamond phosphoprotein gel stain followed by densitometry to determine the relative phosphorylation states. NS2 phosphorylation for mutants A2 and A3 was not significantly different from the wt, however NS2 phosphorylation in mutant A1 was significantly reduced (~70%). The SAA mutant virus showed no phosphorylation in BSR cells as previously reported (Fig. 10) (11). The decrease in phosphorylation in mutant A1 is consistent with the data obtained from *in vitro* phosphorylation experiment and poor Ca^{2+} binding observed from CD (Fig. 5, Fig. 6). These data indicate that poor Ca^{2+} binding, due to disruption of Asp and Glu amino acid residues in Ca^{2+} binding motif (250-253aa), specifically interfere with NS2 phosphorylation in cells infected with Ca^{2+} mutant virus.

Discussion

Several viruses are known to synthesize Ca^{2+}-binding proteins containing EF hand-like motif (28). Our *in-silico* methods predicted the presence of a unique EF hand-like calcium binding motif in NS2, resembling more like a "Ca^{2+} bowl" like structure with clusters of Asp and Glu residues. The absence of a high-resolution structure of full length NS2 limits our understanding of the detailed structural features of the "Ca^{2+}

bowl". Therefore, we have taken a genetic approach to validate the predicted Ca^{2+} binding activity of this region. We tested alanine substitution of these residues by generating recombinant mutant NS2 proteins, A1, A2, and A3 targeting three sites of the putative Ca^{2+} binding region. Our biochemical and biophysical experiments with these mutant proteins demonstrated that NS2 is indeed a Ca^{2+} binding protein and the binding of Ca^{2+} to the negatively charged residues in the A1 site (aa 250-253) is highly specific. Our data also suggest that this unusual "Ca^{2+} bowl" like motif of NS2 acts as a Ca^{2+} sensor. In addition, in the presence of a specific chelating agent such as EGTA, the CD spectrum of NS2-Ca^{2+} was partially reversed. Further, like several other CaBP, NS2 also demonstrated a contrasting change in the percentage of helix in NS2 (helix-to-coil) upon Ca^{2+} binding in far UV-CD spectroscopic measurements. The Ca^{2+} concentrations used in the far UV-CD experiments was to a 1:1 stoichiometry (approximately) with NS2, which is a decamer in purified form. More importantly when we introduced the same mutations in the NS2 encoding gene of replicating viral genome, A1 mutation failed to recover infectious virus and plaque formation, reflecting the importance of the Ca^{2+} sensing activity of NS2 for the production of infectious virus.

To investigate the mechanism behind failure of virus recovery, we tested effect of calcium binding mutants on the phosphorylation state of NS2 protein both *in vitro* (recombinant NS2 protein) and *in vivo* (NS2 expressed by mutant virus particles in cells). In our *in vitro* kinase assay, the level of phosphorylation was increased in the presence of Ca^{2+}, indicating that Ca^{2+} mediated changes in secondary structural elements in NS2 might have led to better access to the phosphorylation sites to the enzyme. The data from the kinase assay was consistent with the CD data on Ca^{2+} mediated changes in secondary structural elements (helix) in NS2. These Ca^{2+} induced changes in NS2 is significant, although it does not appear to destabilize its oligomeric state, as revealed by cryo-EM analysis and size exclusion chromatography. This suggests that it is the oligomeric NS2 that senses the Ca^{2+} ions possibly through coordination between the protomers rather than individual monomeric subunits independently sensing Ca^{2+} ions and forming a decamer. Interestingly, a ring-like shape was inferred for full-length NS2 based on negative-stain electron microscopy (29). In this study, CryoEM analysis of full-length NS2 shows that the subunits are arranged in helical configuration (10 subunits / pitch). *In vivo*, similar effects on phosphorylation state of NS2 in cells infected with mutant virus suggests crucial role

of NS2 in host's calcium homeostasis, which possibly is linked to the wider role of NS2 in VIB assembly/disassembly.

Several viral proteins are reported to alter cellular calcium homeostasis to assist viral life cycle, by modulating mainly membrane-associated Ca^{2+} pumps. For instance, HBx of HBV, modulate Ca^{2+} pumps at the plasma membrane (30), viral proteins such as Vpr (HIV-1) modulates Ca^{2+} pumps associated with mitochondrial membranes (31) and NSP4 of rotavirus (*Reoviridae*) do the same to Ca^{2+} pumps at the Endoplasmic Reticulum (32). It is noteworthy that although NS2 is largely cytosolic not localising to any membrane, yet it demonstrates significant potential to manipulate host's Ca^{2+} signaling through characteristic calcium binding motif (EF hand-like) during the assembly of VIBs, the viral assembly factories.

Specifically, different members of *Reoviridae* family also form similar VIB-like structures (referred as viral factories or viroplasms in rotavirus/reovirus), although each having their own unique features (33,34). One of the important regulatory factors critical for VIBs/viroplasms assembly is phosphorylation of viral proteins, such as NSP2 of rotavirus and NS2 of BTV, which controls self-oligomerization of VIB-forming viral proteins (2,33). Thus, our study provides further insights on the mechanism behind the regulation of this phosphorylation of VIB forming protein NS2 in BTV. We found that Ca^{2+} binding preferentially affects phosphorylation level of the NS2, suggesting the broader relevance of NS2 in the context of modulating Ca^{2+} related signaling. During VIB assembly in the infected cells, phosphorylated NS2 is produced abundantly and its level can be correlated with the abundance of CaBP calmodulin. These NS2 molecules play multiple roles such as recruiting different RNA segments, self-oligomerization forming large inclusion bodies for replication and viral genome packaging. The complex mechanism of assembly and disassembly of VIBs must be reversible and precisely regulated such that it is in sync with several other cellular processes, which is necessary to avoid any aggregate formation within the host cells during the assembly/disassembly.

Ca^{2+} signaling controls diverse cellular processes. Understanding the details of NS2-Ca^{2+} interaction greatly expands our knowledge of VIB assembly and disassembly in the context of calcium homeostasis of the cell (35-41). Although the details of the complex mechanism of VIB assembly is not well understood, the importance of phosphorylation of NS2 in VIB assembly was clearly demonstrated in our earlier study where mutations of serine residues S249, S259 (phosphorylation site)

aborted VIB assembly (2). In light of our current data, we propose a model of NS2 mediated VIB assembly in which the Ca^{2+} sensing activity of NS2 is linked to its phosphorylation status (2,11), which in turn control the VIB assembly required for virus replication and genome packaging.

Materials and Methods

Construction of expression plasmids, protein purification and gel filtration

Based on the SMART motif search results (12), the plasmids for NS2 mutants were generated by the QuikChange mutagenesis method (Agilent Technologies) from the expression plasmids pET 15b-NS2 for bacterial expression and pCAG NS2 for mammalian cell expression (27,42). Plasmids used for reverse genetics were pCAGGS BTV1 protein expression plasmids (pCAG-VP1, pCAG-VP3, pCAG-VP4, pCAG-VP6, pCAG-NS2) and T7 plasmids for BTV transcripts as previously described (27). Site-directed mutagenesis of BTV1 NS2 was performed in both T7 plasmid for segment 8 (encoding NS2) template, pET15b-NS2 and pCAG-NS2 template, using the following mutagenic primers (5'−3'): $DDD_{250\text{-}2}AAA$ (AGGTGAAGACTCTGAGTGCCGCTGCTGAACAAGGTGAGGATGC), $ED_{256\text{-}7}AA$ (CGATGATGAACAAGGTGCGGCTGCGAGTGACGATGAAC) and $DDE_{260\text{-}2}AAA$ (CAAGGTGAGGATGCGAGTGCCGCTGCACACCCAAAAACTCATA). Obtained mutants were sequenced using internal NS2 primers in order to confirm the presence of the desired mutation(s). The wild type NS2 and mutant proteins were expressed in the *E. coli* bacteria strain BL21 (DE3) pLysS. The culture was grown at 37 °C until OD_{600} nm reached 0.5-0.6 and induced with 0.5 mM IPTG. The bacterial cultures were grown at 37 °C for the next 4 hours, post induction. Cells were then lysed for the protein purification. The Ni-NTA affinity purification was used, to purify the wild type and mutant proteins eluting in the presence of 250 mM Imidazole (Elution buffer: 20mM Tris-HCl, 150 mM NaCl, pH 7.4, 250 mM Imidazole). In order to remove traces of nucleic acid from the purified protein, samples were treated with Benzonase® Nuclease or Micrococcal Nuclease where necessary. For gel filtration Superdex® 200 10/300 GL (GE/Cytiva) column was used in running buffer 20 mM HEPES, 100mM NaCl, pH 7.4 at the flow rate of 0.2 mL per minute.

Circular dichroism

The circular dichroism (CD) spectra of wild type apo NS2 (treated with Chelex-100 resin, Bio-Rad) were recorded in CD buffer (20 mM HEPES, 100mM NaCl, pH 7.4) at room temperature (20 °C). All buffers were pre-treated with Chelex-100 resin to remove divalent metal ions contaminants. For Calcium binding studies the apo NS2 sample was titrated with Ca^{2+} salts in increasing concentration. Far ultra-violet (UV) CD spectrum data were collected from 260 –195 nm with a 0.5 mm rectangular cell path length at 20 °C on the Applied Photophysics Chirascan & Chirascan Plus spectrometers (Leatherhead, UK) attached to a Peltier unit (Quantum NorthWest TC125). The UV & CD spectra were smoothed (window factor of 4, Savitzky-Golay method) and analyzed using Origin V6 and APL Prodata Viewer v4.2.15. For comparative metal ion titration experiments, same preparation of wtNS2 protein sample was aliquoted in two halves just before titration on CD instrument. Equal amount of Ca^{2+} and Mg^{2+} were added to each tube respectively in the increasing concentrations to obtain same concentrations for two metal ions. The Ca^{2+} or Mg^{2+} concentrations were taken from 5 µM to 10 mM range. For Kd measurement CD_{222nm} was plotted (Y axis) for each Ca^{2+} concentrations (X-axis) and Kd value was derived using Graphpad Prism choosing inbuilt one-site total function for nonlinear regression (curve fit). Likewise, similar concentrations of mutant proteins A1, A2, A3 were used for titration and similar Ca^{2+} concentration range (5µM to 10mM) was studied.

In vitro kinase assay with [γ-^{32}P] – ATP

For the kinase assay, substrate protein NS2 (6X-His tag) and kinase enzyme CK2 (GST tag) were expressed separately in *E.coli* cells and purified using nickel and glutathione sepharose respectively. The kinase reaction was conducted in a 50 µL of reaction-mixture volume in 1X reaction buffer (20mM Tris, 100mM NaCl, pH 7.4, 1mM DTT). The reaction tubes were prepared by adding two different concentrations of Mg^{2+} or Ca^{2+} while keeping the substrate (0.7mg/mL) and enzyme (0.4mg/mL) concentrations unchanged. For another tubes different mutants of NS2 was added with Ca^{2+}. The reaction was started by adding 10 µCi of γ-[^{32}P] ATP (Pekin Elmer, 250 µCi) and 0.5mM ATP in each tube at the interval of 15s. Additional 1X buffer was added to the tubes to adjust the dilution factor and making each tube up to 50 µL of reaction volume. The reaction tubes were then incubated for 30 minutes at 37 °C. After incubation, the reaction tube was boiled in SDS sample buffer and loaded

437 on SDS-PAGE to run at 90V 3 hours. The SDS-PAGE gel was then dried, exposed
438 to film and observed under imager.
439
440 **CryoEM sample preparation, image collection and data processing**
441 For cryoEM, 2.5 µL of NS2 in 20mM Tris, 150mM NaCl, pH 7.4, supplemented with
442 0.1mM $CaCl_2$), was applied to thin continuous carbon film on lacey grid (Ted Pella)
443 and blotted using a Vitrobot Mark IV (Thermo Fisher Scientific) with the standard
444 Vitrobot filter paper at 4°C. The blotting time was set to 6 s, blotting force was set to
445 2 and drain time was set to 1s. The grid was flash-frozen in liquid ethane and stored
446 in liquid nitrogen. 2,712 micrographs were collected on a Titan Krios 300 kV electron
447 microscope (Thermo Fisher Scientific) equipped with a Gatan imaging filter (GIF)
448 Quantum LS and a Gatan K2 Summit direct electron detector operated in super-
449 resolution mode at magnification of 130K (calibrated pixel size of 0.535 Å on the
450 sample level). The GIF slit width was set to 20 eV. The dose rate on the camera was
451 set to ~6.5 electrons/pixel/s. The total exposure time of each movie was 8 s, which
452 fractionated into 40 frames of images with 0.2 s exposure time for each frame. Dose-
453 fractionated frames were 2x binned (pixel size 1.07 Å) and aligned for beam-induced
454 drift correction using UCSF MotionCorr2 (43). The defocus values of the
455 micrographs were determined by CTFFIND4 (44) to be in the range of -1.0 µm and -
456 4.0 µm. From a total of 2,712 micrographs, 463,691 particles were boxed out in 400
457 x 400 square pixels and 2x binned to 200 x 200 square pixels (pixel size of 2.14 Å) to
458 speed up further data processing with RELION 3.0 (45). After one round of 2D
459 classification,159,361 particles (34.4% of all particles) were selected and subjected
460 to the second round of 2D classification. Represented 2D classes are selected and
461 used for the measurement of pitch and diameter of spiral NS2 oligomers.

462 **Cells, viruses and reverse genetics**
463 BSR cells (BHK-21 subclone) or BS8 (BSR cells stably expressing NS2/Segment of
464 BTV) were cultured in Dulbecco's modified Eagle's medium (DMEM) supplemented
465 with 5% (v/v) fetal bovine serum (FBS) at 35°C in 5% CO2. Media for BS8 was also
466 supplemented with puromycin. Each mutant and wild type virus were recovered (either
467 from BSR or BS8 cells) by reverse genetics as previously described (27). Each
468 recovered virus was plaque-purified, amplified and titrated using plaque assay. For
469 reverse genetics: Synthetic single-stranded RNAs were prepared by runoff *in vitro*

transcription from T7 PCR products using T7 RNA polymerase. Transcripts were prepared with anti-reverse cap analogue (ARCA) using mMESSAGE mMACHINE T7 Ultra kit (Ambion) as previously described (27). Reverse genetics was performed as previously described (27). Briefly, at day 1, 70–80% confluent BSR monolayers were transfected with pCAG-VP1, pCAG-VP3, pCAG-VP4, pCAG-VP6 and wild-type or mutated pCAG-NS2 (120 ng each) using Endofectin (GeneCopoeia), according to the manufacturer's instructions and incubated at 35°C in 5% CO2 overnight. At day 2, the cells were transfected with each BTV1 exact copies RNA transcripts (S8 wild-type or mutated) using Endofectin (GeneCopoeia), overlaid with 1% agarose and incubated 3 days at 35°C in 5% CO2. Visible plaques were picked up and resuspended in 1% FBS containing medium, and/or cells were subsequently fixed with 10% formaldehyde and stained with crystal violet. Each recovered virus was plaque-purified, amplified and harvested 3 days post infection. Viruses were titrated using plaque assay.

Immunofluorescence and VIB analysis from microscopy data

BSR cells were grown on coverslips and infected at MOI 1 (Multiplicity of infection) with NS2 wild-type or mutant recovered viruses. Twenty-four hours post infection cells were fixed with 4% paraformaldehyde (Sigma-Aldrich) solution, permeabilized with 0.5 % Triton X100 (Sigma), blocked with 1% BSA (Bovine Serum Albumin, Sigma), and subsequently stained using a guinea pig anti-NS2 primary antibody (lab made) and an anti-guinea pig Alexa 488 coupled secondary antibody (Thermo Fisher Scientific). Nuclei were stained using Hoechst 33342 (Thermo Fisher Scientific). Images were acquired using an x100 oil objective and a Zeiss Axiovert LSM880 confocal microscope supplied with the Zen software. For each infection condition (wild type virus versus A1, A2 or A3 mutant viruses, Table 1), five fields were randomly selected and z-stacks (14 to 19 slices) were acquired (x:1912, y:1912, 12-bit). Each field contained in average 17 infected cells, and the experiment was repeated three times independently. Maximum intensity projection of each z-stack was performed using the Zen software and obtained images were further processed using the ImageJ software (version 1.52a, http://imagej/nih.gov/ij). Only particles (i.e., VIBs) with a size > 0.5µm^2 were selected for particle analysis. The experiment was performed three times and in total 1600 VIBs were used for the wild-type virus, 764 VIBs for the DDD$_{250\text{-}2}$AAA mutant, 1534 VIBs for the ED$_{256\text{-}7}$AA mutant and 1597 VIBs for the DDE$_{260\text{-}2}$AAA mutant virus respectively.

Immuno-precipitation and Phosphoprotein staining

NS2 was purified from BTV1 infected BSR cells (MOI=1) after 18 hours. Cells were washed with PBS before lysis. Cells were lysed in lysis buffer (50 mM Tris-HCl (pH 7.5), 125 mM NaCl, 5 % Glycerol, 0.2 % NP-40, 1.5 mM MgCl2, 25 mM NaF, 1 mM Na3VO4, 1 mM Beta-glycerophosphate, 10 mM sodium pyrophosphate and protease inhibitor) for 30 minutes on ice. Lysates were centrifuged at 800g for 15 minutes. Supernatants were recovered and added to protein A sepharose beads conjugated to Guinea-pig anti-NS2 and were incubated on ice overnight. Samples were centrifuged at 2,000g for 2 minutes. The supernatant was removed and the protein A sepharose beads washed with lysis buffer. Samples were centrifuged at 2,000g for 2 minutes. This wash process was repeated 4 times. SDS loading buffer was then added to the protein A sepharose beads before being boiled. SDS-PAGE gels were stained with Pro-Q Diamond phosphoprotein gel stain (ThermoFisher). For stain, the respective fluorescence was detected and quantified.

Acknowledgement

We thank I. M Jones (University of Reading, United Kingdom) for critically reviewing the manuscript. We are grateful to Tam Bui of the Bimolecular Spectroscopy Centre, King's College London, who helped with the collection of CD data. This work was supported by the U.S. National Institutes of Health (NIH R01AI094386 to ZHZ and PR) and partly by the Wellcome Trust, UK (WT100218; Investigator Award to P.R.). We acknowledge the use of instruments at the Electron Imaging Center for Nanomachines supported by UCLA and grants from NIH (1S10OD018111 and 1U24GM116792) and NSF (DBI-1338135 and DMR-1548924).

Conflict of interest

The authors declare no conflict of interest with the contents of this article.

Author Contributions

SKR, PR designed the experiments; SKR, AK, BPM and YH performed the experiments; SKR, PR and ZHZ analysed data. SKR, PR and ZHZ wrote the manuscript.

538 **References**

539

540 1. Beaton AR, Rodriguez J, Reddy YK, Roy P. 2002. The membrane trafficking
541 protein calpactin forms a complex with bluetongue virus protein NS3 and
542 mediates virus release. Proc Natl Acad Sci USA. 99(20): 13154-12159.
543 2. Modrof J, Lymperopoulos K, Roy P. 2005. Phosphorylation of bluetongue virus
544 nonstructural protein 2 is essential for formation of viral inclusion bodies. J Virol.
545 79(15): 10023-10031.
546 3. Kerviel A, Ge P, Lai M, Jih J, Boyce M, Zhang X, Zhou ZH, Roy P. 2019. Atomic
547 structure of the translation regulatory protein NS1 of bluetongue virus. Nat
548 Microbiol. 4(5): 837-845.
549 4. Belhouchet M, Mohd JF, Firth AE, Grimes JM, Mertens PP, Attoui H. 2011.
550 Detection of a fourth orbivirus non-structural protein. PLoS One. 6 (10):e25697.
551 5. Ratinier M, Caporale M, Golder M, Franzoni G, Allan K, Nunes SF, Armezzani
552 A, Bayoumy A, Rixon F, Shaw A, Palmarini M. 2011. Identification and
553 characterization of a novel non-structural protein of bluetongue virus. PLoS
554 Pathog. 7(12): e1002477.
555 6. Stewart M, Hardy A, Barry G, Pinto RM, Caporale M, Melzi E, Hughes J,
556 Taggart A, Janowicz A, Varela M, Ratinier M, Palmarini M. 2015.
557 Characterization of a second open reading frame in genome segment 10 of
558 bluetongue virus. J Gen Virol. 96(11): 3280-3293.
559 7. Celma CC, Roy P. 2011. Interaction of calpactin light chain (S100A10/p11) and
560 a viral NS protein is essential for intracellular trafficking of nonenveloped
561 bluetongue virus. J Virol. 85(10): 4783-4791.
562 8. Zocchi MR, Rubartelli A, Morgavi P, Poggi A. 1998. HIV-1 Tat inhibits human
563 natural killer cell function by blocking L-type calcium channels. J Immunol.
564 161(6): 2938-2943.
565 9. Bowman GD, Nodelman IM, Levy O, Lin SL, Tian P, Zamb TJ, Udem SA,
566 Venkataraghavan B, Schutt CE. 2000. Crystal structure of the oligomerization
567 domain of NSP4 from rotavirus reveals a core metal-binding site. J Mol Biol.
568 304(5): 861-871.
569 10. Matsuo E, Roy P. 2013. Minimum requirements for bluetongue virus primary
570 replication *in vivo*. J Virol. 87(2): 882-889.

11. Mohl BP, Roy P. 2016. Cellular Caesin Kinase 2 and Protein Phosphatase 2A Modulate Replication Site Assembly of Bluetongue Virus. J Biol Chem. 291(28): 14566-14574.
12. Letunic I, Bork P. 2018. 20 years of the SMART protein domain annotation resource. Nucleic Acids Res. 46(D1): D493-D496.
13. Schafer BW, Heizmann CW. 1996. The S100 family of EF-hand calcium binding proteins: functions and pathology. Trends Biochem Sci. 21(4): 134-140.
14. Grabarek, Z. 2006. Structural basis for diversity of the EF-hand calcium-binding proteins. J Mol Biol. 359(3): 509-525.
15. Nakayama S, Kretsinger RH. 1994. Evolution of the EF-hand family of proteins. Annu Rev Biophys Biomol Struct 23: 473-507.
16. Bian S, Favre I, Moczydlowski E. 2001. Ca^{2+} binding activity of a COOH-terminal fragment of the Drosophila BK channel involved in Ca^{2+} dependent activation. Proc Natl Acad Sci U S A. 98(8): 4776-4781.
17. Niu X, Magleby KL. 2002. Stepwise contribution of each subunit to the cooperative activation of BK channels by Ca^{2+}. Proc Natl Acad Sci U S A. 99(17): 114411-11446.
18. Bao L, Kaldany C, Holmstrand EC, Cox DH. 2004. Mapping the BKCa channel's Ca^{2+} bowl: side-chains essential for Ca^{2+} sensing. J Gen Physiol. 123(5): 475-489.
19. Yusifov T, Savalli N, Gandhi CS, Ottolia M, Olcese R. 2008. The RCK2 domain of the human BKCa channel is a calcium sensor. Proc Natl Acad Sci U S A. 105(1): 376-381.
20. Chazin WJ. 2011. Relating form and function of EF-hand calcium binding proteins. Acc Chem Res. 44(3): 171-179.
21. Kawasaki H, Kretsinger RH. 2017. Structural and functional diversity of EF-hand proteins: Evolutionary perspectives. Protein Sci. 26(10): 1898-1920.
22. Zhang M, Tanaka T, Ikura M. 1995. Calcium-induced conformation transition revealed by the solution structure of apo calmodulin. Nat Struct Biol Sep; 2(9): 758-767.
23. Jones DT. 1999. Protein secondary structure prediction based on position-specific scoring matrices. J Mol Biol. 17;292(2):195-202.

24. Mészáros B, Erdos G, Dosztányi Z. 2018. IUPred2A: context-dependent prediction of protein disorder as a function of redox state and protein binding. Nucleic Acids Res. 46(W1): W329-W337.
25. Micsonai A, Wien F, Bulyáki É, Kun J, Moussong É, Lee YH, Goto Y, Réfrégiers M, Kardos J. 2018. BeStSel: a web server for accurate protein secondary structure prediction and fold recognition from the circular dichroism spectra. Nucleic Acids Res. 46(W1): W315-W322.
26. Butan C, Van Der Zandt H, Tucker PA. 2004. Structure and assembly of the RNA binding domain of bluetongue virus non-structural protein 2. J Biol Chem. 279(36): 37613-37621.
27. Celma CC, Roy P. 2009. A viral nonstructural protein regulates bluetongue virus trafficking and release. J Virol. 83(13): 6806-6816.
28. Zhou Y, Frey TK, Yang JJ. 2009. Viral Calciomics: Interplays Between Ca^{2+} and Virus. Cell Calcium. Jul;46(1):1-17.
29. Mumtsidu E, Makhov AM, Roessle M, Bathke A, Tucker PA. 2007. Structural features of the Bluetongue virus NS2 protein. J Struct Biol. 160(2): 157-167.
30. Chami M, Ferrari D, Nicotera P, Paterlini-Brechot P, Rizzuto R. 2003. Caspase-dependent alterations of Ca^{2+} signaling in the induction of apoptosis by hepatitis B virus X protein. J Biol Chem. 278(34): 31745-31755.
31. Jacotot E, Ravagnan L, Loeffler M, Ferri KF, Vieira HL, Zamzami N, Costantini P, Druillennex S, Hoebeke J, Briand JP, Irinopoulou T, Daugas E, Susin SA, Cointe D, Xie ZH, Reed JC, Roques BP, Kroemer G. 2000. The HIV-1 viral protein R induces apoptosis via a direct effect on the mitochondrial permeability transition pore. J Exp med. 191(1): 33-46.
32. Crawford SE, Hyser JM, Utama B, Estes MK. 2012. Autophagy hijacked through Viroporin-activated calcium/calmodulin-dependent kinase kinase-beta signaling is required for rotavirus replication. Proc Natl Acad Sci U S A. 109(50): E3405-3413.
33. Criglar JM, Anish R, Hu L, Crawford SE, Sankaran B, Prasad BVV, Estes MK. 2018. Phosphorylation cascade regulates the formation and maturation of rotavirus replication factories. Proc Natl Acad Sci U S A. 115(51): E12015-E12023.

635 34. Crawford SE, Criglar JM, Liu Z, Broughman JR, Estes MK. 2019. COPII
636 Vescicle Transport is Required for Rotavirus NSP4 Interaction with the
637 Autophagy Protein LC3 II and Trafficking to Viroplasms. J Virol 9: 01341-01319.
638 35. Berridge MJ, Bootman MD, Roderick HL. 2003. Calcium signalling: dynamics,
639 homeostasis and remodeling. Nat Rev Mol Cell Biol. 4(7): 517-529.
640 36. Pinton P, Giorgi C, Siviero R, Zecchini E, Rizzuto R. 2008. Calcium and
641 apoptosis: ER-mitochondria Ca^{2+} transfer in the control of apoptosis.
642 Oncogene. 27(50): 6407-6418.
643 37. Harr MW, Distelhorst CW. 2010. Apoptosis and autophagy: decoding calcium
644 signals that mediate life or death. Cold Spring Harb Perspect Biol. 2(10):
645 a005579.
646 38. Pinto MC, Kihara AH, Goulart VA, Tonelli FM, Gomes KN, Ulrich H, Resende
647 RR. 2015. Calcium signaling and cell proliferation. Cell Signal. 27(11): 2139-
648 2149.
649 39. Li B, Tadross MR, Tsien RW. 2016. Sequential ionic and conformational
650 signaling by calcium channels drives neuronal gene expression. Science.
651 351(6275): 863-867.
652 40. Goonawardane N, Gebhardt A, Bartlett C, Pichlmair A, Harris M. 2017.
653 Phosphorylation of Serine 225 in Hepatitis C Virus NS5A Regulates Protein-
654 Protein Interactions. J virol. 91(17). (pii): JVI.00805-00817.
655 41. Takeshita N, Evangelinos M, Zhou L, Serizawa T, Somera-Fajardo RA, Lu L,
656 Takaya N, Nienhaus GU, Fischer R. 2017. Pulses of Ca (2+) coordinate actin
657 assembly and exocytosis for stepwise cell extension. Proc Natl Acad Sci U S
658 A. 114(22): 5701-5706.
659 42. Niwa H, Yamamura K, Miyazaki J. 1991. Efficient selection for high-expression
660 transfectants with a novel eukaryotic vector. Gene. 108(2): 193-199.
661 43. Zheng SQ, Palovcak E, Armache JP, Verba KA, Cheng Y, Agard DA. 2017.
662 MotionCor2: anisotropic correction of beam-induced motion for improved cryo-
663 electron microscopy. Nat Methods. 14(4): 331-332.
664 44. Rohou A, Grigorieff N. 2015. CTFFIND4: Fast and accurate defocus estimation
665 from electron micrographs. J Struct Biol. 192(2): 216-221.
666 45. Scheres SH. 2012. RELION: implementation of a Bayesian approach to cryo-
667 EM structure determination. J Struct Biol. 180(3): 519-530.
668

669 **Table 1: Alanine substitution mutations of NS2**

Alanine mutants	Abbreviations
$S_{249}A + S_{259}A$	SAA
$DDDE_{250\text{-}3}AAAA$	A1
$ED_{256\text{-}7}AA$	A2
$DDE_{260\text{-}2}AAA$	A3
$DDDE_{250\text{-}3}AAAA + ED_{256\text{-}7}AA$	A1+ 2
$DDDE_{250\text{-}3}AAAA + ED_{256\text{-}7}AA + DDE_{260\text{-}2}AAA$	A 1+2+3

670

671 **Figure legends**

672 **Figure 1: Sequence analysis of the BTV1 NS2 protein. (A)** Amino acid sequence
673 of NS2 (residues 204-300) with signature residues of the EF hand motif highlighted in
674 bold and location of the three putative calcium binding sites (A1, A2, A3) containing
675 Aspartic acid and Glutamic acid residues are indicated. (**B)** Amino acid sequence
676 alignment showing the conservation of the three putative calcium binding sites in NS2
677 among 24 different BTV serotypes.

678 **Figure 2: Calcium binding by NS2 and its oligomeric state.** Purified NS2 was pre-
679 treated with Chelex 100 resin and then incubated with different Ca^{2+} concentrations (5
680 µM to 10 mM range) and analysed by circular dichroism. **(A)** The NS2 protein was
681 expressed in *E. coli* and analysed by SDS-PAGE gel followed by Coomassie blue
682 staining. M is the molecular mass markers as shown. **(B)** Far UV CD spectra of Ca^{2+}
683 titration binding by NS2 protein represented in Log 10 scale. Binding constant (Kd)
684 values of NS2 protein with Ca^{2+} (Kd = 53.9 ± 8.4 **µM**, red) and Mg^{2+} (Kd = 2.48 ± 0.4
685 **mM**, black). (**C)** The plot of Ca^{2+} titration binding in linear scale to show saturation
686 points. **(D)** Size exclusion chromatography showing both apo NS2 (grey line) and in
687 presence of Ca^{2+} (red line), were eluted at the elution volume corresponding to a
688 marker protein of 440 kDa.

689 **Figure 3: Helix-to-Coil transition of NS2 in presence of Ca^{2+}.** Analysis of CD
690 spectra in presence of Ca^{2+} (**A)** Far UV spectrum of 8.3 µM NS2 apo alone (green
691 line), in the presence of 0.66 µM Ca^{2+} (red line), and in the presence of 0.66 µM Ca^{2+}
692 and 0.4µM EGTA (cyan line). (**B)** Far UV spectrum of 5.5 µM NS2 apo alone (green),
693 in the presence of 4.67 µM Ca^{2+} (orange) and in the presence of 44.67 µM Ca^{2+} (red).

694 **Figure 4: Secondary structure prediction of purified wildtype and Ca^{2+}mutant**
695 **NS2 proteins**. (**A)** Secondary structure prediction of NS2 using PSIPRED (23)

showing amino acid regions for predicted beta strand (yellow), helix (pink) and coil (grey). **(B)** Intrinsic unfolded regions predicted by IUPred2 (24) shows high propensity of unfolding near and at Ca^{2+} site (black line). X-axis is amino acid positions and Y-axis is probability score 0 to 1. (**C)** Coomassie blue stained SDS-PAGE of the wt and NS2 mutant proteins. M is the molecular mass markers.

Figure 5: CD spectra and Ca^{2+} binding by NS2 mutants. Purified wtNS2 and mutants A1, A2, A3 were analysed by circular dichroism **(A)** Comparative far UV CD spectra of wtNS2 (black circles) and mutants A1 (red), A2 (green), A3 (cyan). **(B)** Estimation of percent secondary structure contents from far UV CD spectra (n=3). Other predicted secondary structure elements such as, 3-10 helix, bends, irregular/loops, π-helix are represented as "others". A star (*) denotes a significant difference from control ($P < 0.05$) (n=3) **(C)** Far UV CD spectra of Ca^{2+} titration binding by NS2 mutant proteins represented in Log 10 scale. The Kd (μM) values of mutants A3 (Kd = 44 ± 2.4, cyan), A2 (Kd = 64 ± 1.8, green) and A1 (Kd = 150 ± 3.2, red). **(D)** is the plot of Ca^{2+} titration in linear scale to show saturation points.

Figure 6: Phosphorylation of NS2 increases in the presence of calcium during *in vitro* kinase assay. Phosphorylation levels of NS2 by CK2 kinase was determined by the intensity of **γ-^{32}P** signal transferred to NS2. (**A)** wtNS2 phosphorylation levels in the absence of CK2α (negative control, -ve), with CK2α before metal binding (Apo) and in the presence of Mg^{2+} and Ca^{2+}. Phosphorylation levels in NS2 mutants A1, A2 and A3 in presence of Ca^{2+}. NS2 loading control is shown in lower panel (**B)** NS2 phosphorylation levels in the presence of different concentrations (1μM, 2μM) of Mg^{2+} (left) and Ca^{2+} (right). Both blots were scanned together (**C)** Densitometry analysis of blot, for wild type NS2 and mutants in presence of Ca^{2+}, from (A)**.** The P value was determined from the t – test of values for γ-^{32}P intensity (n=3).

Figure 7. Cryo-electron microscopy of NS2 oligomer. (**A-B)** Representative class averages of cryo-EM side (A) and front (B) views of NS2. The pitch and diameter of NS2 helix are measured based on the 2D class average results. (**C**) Ribbon and surface representations of oligomeric NS2 N-terminal domains. The model is generated based on the crystal structure of NS2 N-terminal domain (PDB: 1UTY, 22) and related crystal packing information. The C-terminal ends of each NS2 N-terminal domain (residue K160) are labelled as purple spheres. (**D**) CryoEM 2D classification result of 159,361 particles. 2D classes of NS2 particles on their side and front views

are boxed in red and yellow, respectively. Numbers 1, 3, 8,16, 20 denote subunits of N-terminal domain.

Figure 8: Disruption of putative Ca^{2+} binding motifs in NS2 affects plaque formation. BSR and BS8 cell monolayers were transfected with wt and each mutant S8 (Ca^{2+} binding site) together with the 9 RNA segments. SAA mutant was used as a negative control and mock was without any transfection. Images show plaques in transfected BSR and BS8 cells.

Figure 9: Viruses mutated in calcium binding motif showed smaller VIBs. (A) Intracellular localization of wt or mutant NS2 24h after infection. Immunofluorescence analysis showed smaller VIBs in cells infected with the mutant A1 as compared to those infected with the wt virus. NS2, green (Alexa 488), Nuclei, blue (Hoechst staining). Scale bars, 20 μm. **(B)** Quantification of the average size of VIBs calculated as area (in μm^2) from the microscopy data (n=3). A star (*) denotes a significant difference from control ($P < 0.05$).

Figure 10: NS2 phosphorylation decreases following disruption of putative Ca^{2+} binding motifs in NS2. Quantification of NS2 phosphoproteins to total proteins staining data from replicate experiments plotted in bar diagram. Error bars represent the SD values from three independent experiments. A star (*) denotes a significant difference from control ($P < 0.05$) (n=3).

A

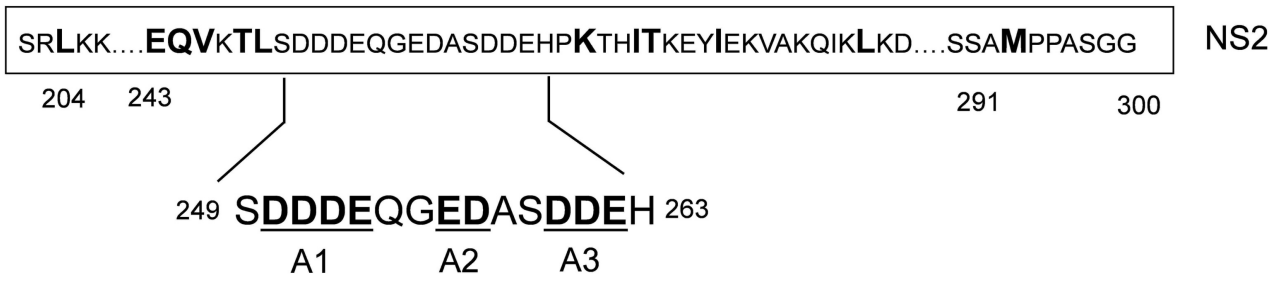

B

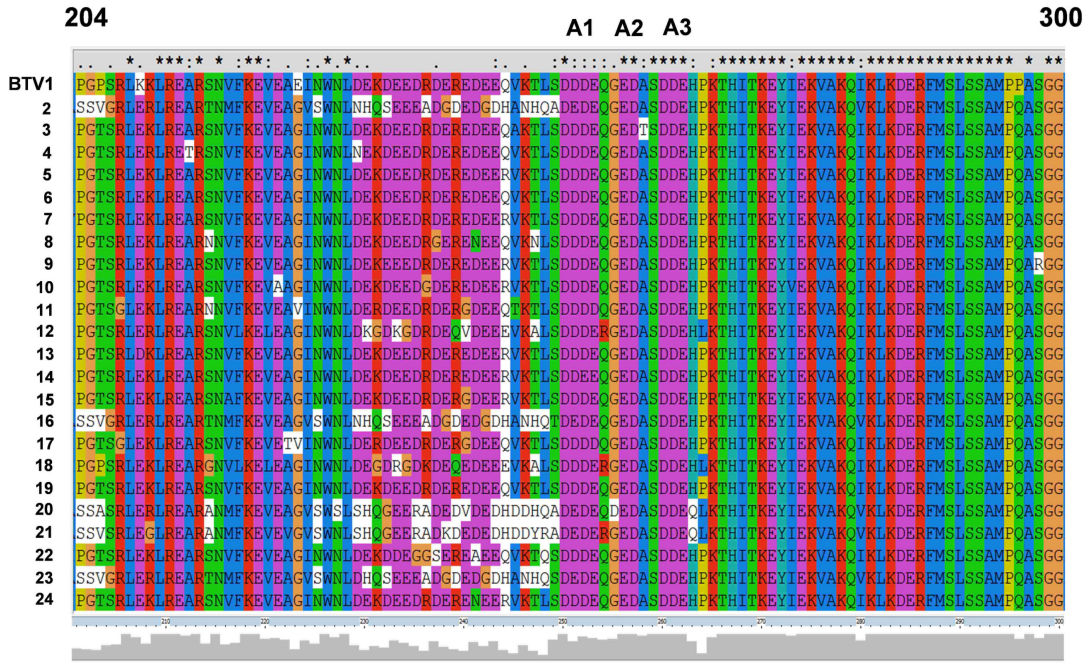

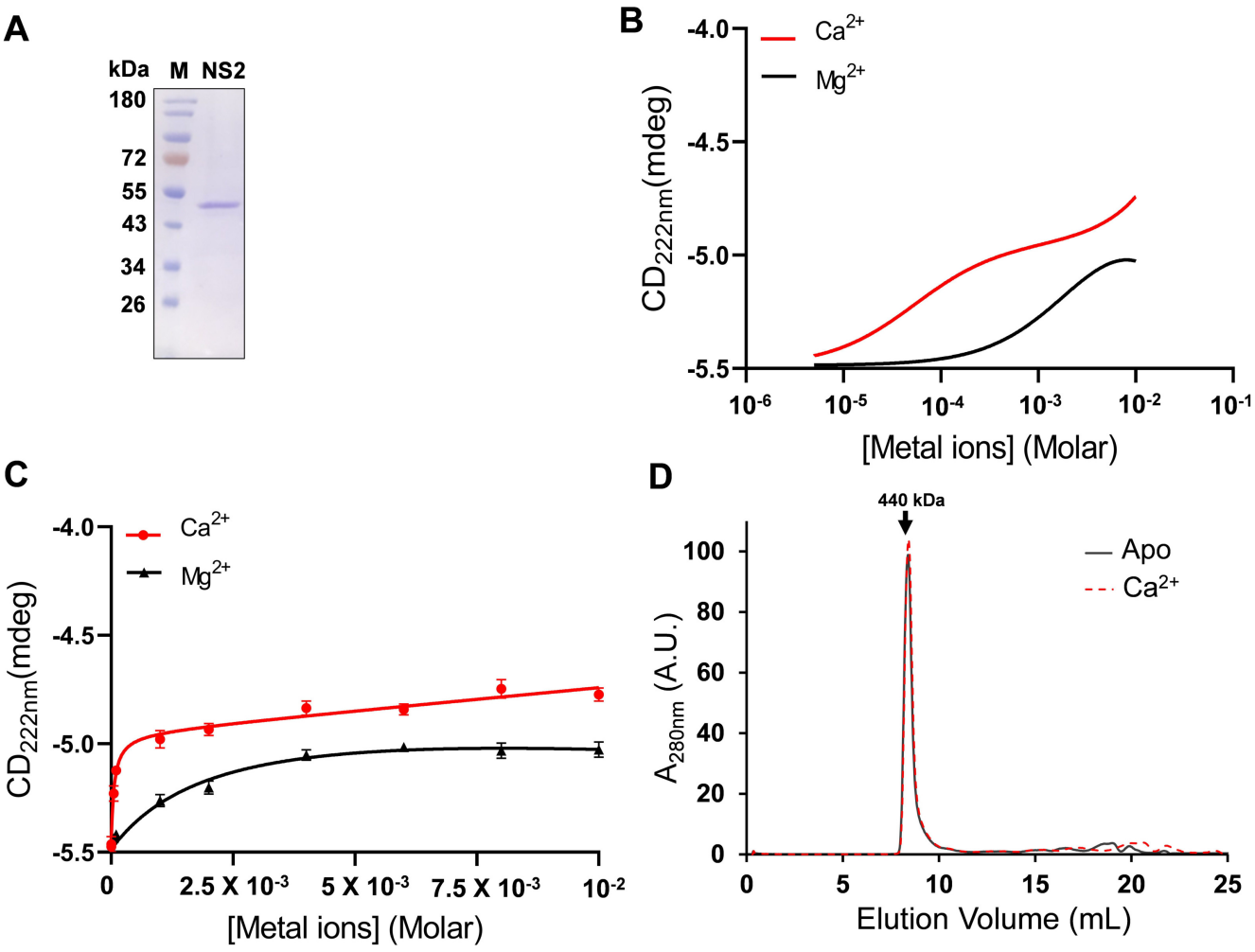

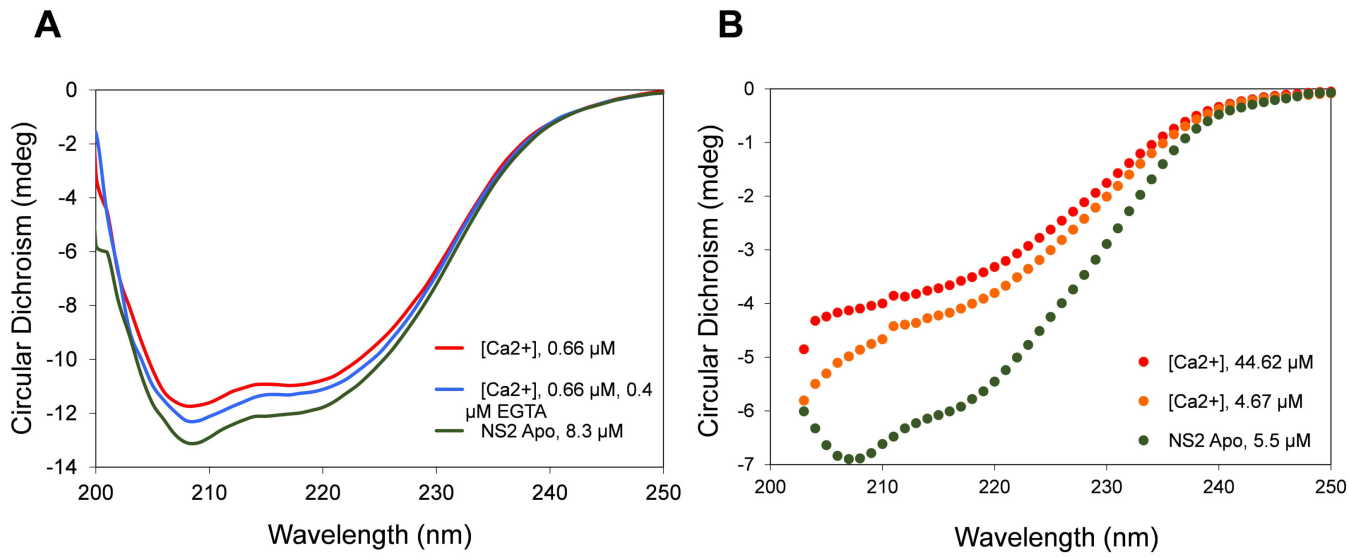

A

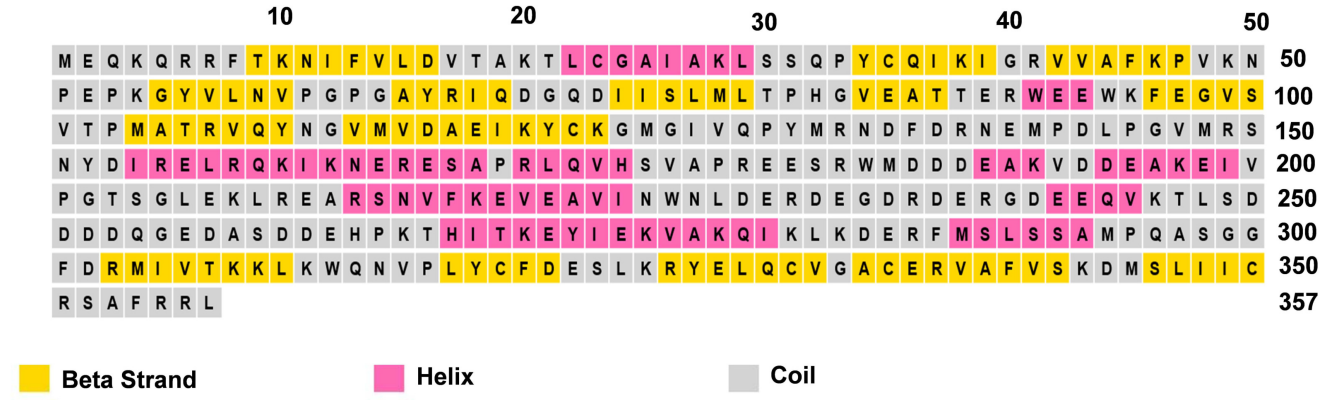

B

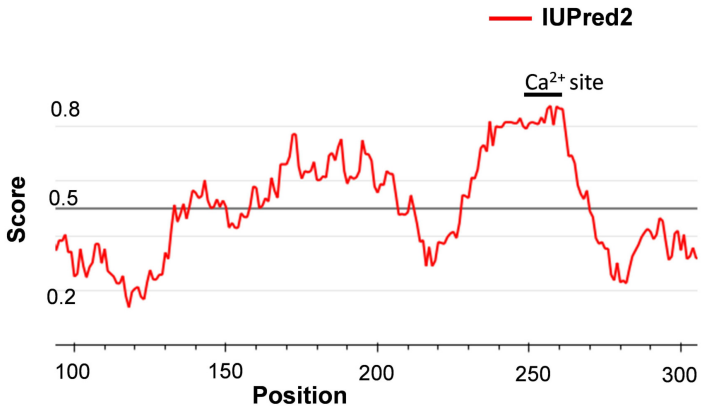

C